Modification of modal characteristics in wakes of square cylinders with multi-scale porosity

J.E. Higham,[1] A. Vaidheeswaran,[2] W. Brevis,[3] and F.C.G.A. Nicolleau, J. Marlow[4]

[1)] *School of Environmental Sciences, University of Liverpool, Liverpool, UK*[a)]

[2)] *US Department of Energy, National Energy Technology Laboratory, 3610 Collins Ferry Rd, Morgantown, WV, USA*

[3)] *Departments of Hydraulics and Environmental & Mining Engineering, Pontifical Catholic University of Chile, Santiago, Chile*

[4)] *Department of Mechanical & Aerospace Engineering, University of Sheffield, Sheffield UK*

Wake flows behind porous patches are complex and host several spatio-temporal features associated with multi-scale excitation. This is in stark contrast to flow past a square cylinder dominated by nonlinear energy cascade stemming from primary vortex shedding instability. In this study, we analyze wakes created by multi-scale patches containing three iterations while maintaining a constant plan porosity. The results are compared to flows obstructed by a square cylinder and a single-scale patch of uniformly distributed elements from the second iteration having the same footprint. Multi-scale porous patches show a protracted wake having a greater spanwise dimension compared to square cylinder. The characteristics are dependent on the arrangement of elements within the patch which effect the extent of bleed flow through the configuration. Besides, we use Proper Orthogonal Decomposition (POD) and Dynamic Mode Decomposition (DMD) to elucidate instability mechanisms at different scales. Distributions of spatial modes reveal element-scale flow structures in the near-wake region with patch-scale turbulence further downstream. Our analysis confirms manipulation of characteristic scales and the associated high-energy events driven by the arrangement of elements within a given patch despite having the same plan porosity.

Keywords: multi-scale wakes; square cylinders; porous patches; fractals; Proper Orthogonal Decomposition;

[a)]Electronic mail: j.e.higham@liverpool.ac.uk

I. INTRODUCTION

Studies on flow past fractal obstructions have always remained relevant because of their occurrence in nature, engineering applications and the built environment we are surrounded by. For instance, cities are often associated with an underlying fractal structure[1–3] which plays a significant role in urban planning and development. Also, the fractal nature of aquatic vegetation protects shorelines by reducing the near-bed velocity[4,5], and improves the quality of water[6–8]. Simplification of such environments in a laboratory setup has led to several published works on flow past idealized obstructions. Extensive research exists on wake structures emanating from circular cylinders[9–13], which was later extended to square cylinders[14–19]. In particular canopies or arrangement of multiple elements have been used to model aquatic vegetations, which have demonstrated sensitivity of wake characteristics to the arrangement of elements and the resulting plan porosity[20–23]. However, majority of work has dealt with patches made from a single scale, i.e., all cylinders have the same dimensions.

We investigate wakes from multiple patches, created from multi-scale square cylinders in the present study. Multi-scale patches can be created having the same plan porosity in an integral sense as a single-scale patch, and contain non-uniform porosity distribution along spanwise cross-sections. The configurations in this study are not to be confused with multi-scale fractal grids[24–30] which have prominently featured in literature over the past couple of decades. Grids are 2-D obstructions placed normal to the streamwise direction having a small finite thickness, while patches used in the current study have standing cylinders on 2-D footprints. Analyses of such multi-scale obstructions are very limited, and are imperative to describe diffusion due to aquatic vegetations or urban developments besides furthering our understanding of turbulence theory.

We use three multi-scale fractal patches designed based on Sierpinski carpet[31], using three iterations. The first (Case V) is a symmetric deterministic patch, while the second is generated by moving the largest iteration to the trailing edge (Case IV). The third is a mirror image of the second (Case III), where the largest iteration is moved to the leading edge. In addition, an array of uniformly spaced single-scale elements corresponding to the second iteration is used (Case II) while maintaining the same plan porosity. The flow-field behind these porous patches are compared with the wake of a square cylinder having the same footprint (Case I). However, there are some noteworthy differences in the underlying

turbulence mechanisms. Square cylinders have instantaneous flow separation at the leading edge, resulting in recirculation zones along their transverse boundaries. Spanwise vortices are present along the transverse edges which get detached and advected downstream forming the von-Karman vortex street. In addition, Wang and Zhou [15] described vortical structures being formed from the base and tip, which interact with the spanwise vortices depending on the geometry and flow conditions, although the latter is absent in our case since the tip is not submerged. In terms of Lagrangian coherent structures (LCS), these vortices are associated with attracting and repelling material lines at the intersection of which saddle points are formed. In the case of a flow past square cylinder, saddle points are formed away from the transverse boundary at high Re_D[32]. Additional saddle points exist in the vicinity of vortex stretching where majority of incoherent turbulence is produced[33].

Wakes behind porous patches are modified by fluid streams bleeding from transverse and trailing edges[22,23]. At sufficiently high porosities, wakes behind individual elements tend to lose their identity and the structure bears resemblance to wake past a solid obstruction albeit being protracted. The decay of perturbations caused by each iteration depends on their dimensions, arrangement and local flow conditions, their effect may diminish within the array or in the near-wake accordingly. Though we maintain the plan porosity across the single-scale and multi-scale patches, we expect the dominant spatial scales in the flow-field to depend on the arrangement of iterations, i.e., porosity distribution. In all the cases considered, additional small-scale structures arise from shear layer instability[33] or interaction between different mechanisms identified in this discussion. It is intuitive that the resulting flow topologies would contain nonlinear interaction of wakes at multiple scales, and traces of material lines and LCS become more convoluted compared to flow past a bluff body. Though LCS offers a different perspective on the evolving flow-field, it is outside the scope of our work presented.

Finally we apply modal decomposition techniques namely, Proper Orthogonal Decomposition (POD)[34–37] and Dynamic Mode Decomposition (DMD)[35,38–40] to elucidate the different instability mechanisms which have also been used to design flow control strategies elsewhere[39,41–46]. Exploring variables in physical space alone may limit our understanding of complex flow dynamics[47–52]. In a strongly nonlinear system containing a broad range of spatio-temporal scales, POD and DMD provides more granularity in characterizing dynamics which might not be apparent while using conventional approaches. In this study,

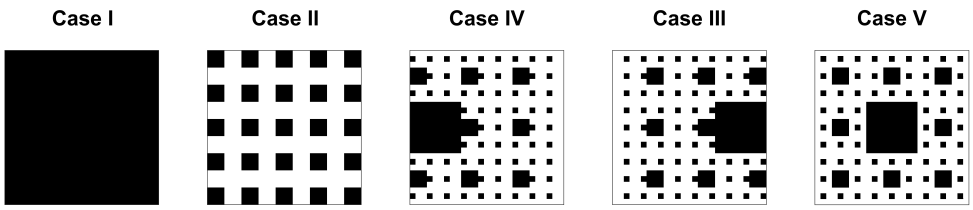

FIG. 1. Cross sections of test Cases used in experiments

we closely examine the first five POD modes ordered based on their modal energy content, and provide observations based on their spatial characteristics. Using spectral information from POD, we extract temporally orthonormal structures through DMD corresponding to the first and second harmonics. The combination of POD and DMD helps in identifying turbulent coherent structures qualitatively which manifest as temporally and spatially relevant features. The remainder of the article is structured as follows: We discuss the experimental setup in Section II and present our results from time-averaged statistics, POD and DMD in Section III followed by concluding remarks in Section IV.

II. EXPERIMENTAL SETUP

Five patches with a cross-sectional area of 162 mm × 162 mm were used as depicted in Figure 1. Case I is a square cylinder, while Case II is a porous patch created from 6 × 6 uniformly spaced 18 mm × 18 mm square rods. To create the multi-scale patches (Cases III-V), finite variants of a Sierpinski carpet with three iterations are used[31]. The largest iteration is present at the leading edge for Case III, trailing edge for Case IV and at the center for Case V. A factor of 3 was used to scale the iterations, with the largest and intermediate iterations measuring 54 mm × 54 mm and 18 mm × 18 mm. The smallest elements measure 6 mm × 6 mm, which were made of 6 mm acrylic sheet laser cut to 0.1 mm precision. The resulting solid fraction in Cases II-V were similar (0.31 in Case II and 0.29 in Cases III-V).

The experiments were undertaken at the University of Sheffield, UK. The patches were placed at the center of an open channel water tunnel and 9 m downstream of the inlet as shown in Figure 2. The transparent flume is 18 m long having a uniform span of 0.49 m. Water from a 25 m^3 tank is fed into the flume using a vibration isolated submersible

pump, and the flow rate is controlled by a solenoid valve. A sluice gate is used at the outlet to maintain the level of water. In our tests, the water on the tunnel was filled up to a height of 0.32 m and the average inlet velocity was set at $U_\infty = 0.19$ m/s. This translates to a cylinder Reynolds number of $Re_D = U_\infty D/\nu = 72405$, and a Froude number of $Fr = U_\infty/\sqrt{gD} = 0.10$. D is the edge length of the footprint, while ν and g, represent kinematic viscosity of water (1.3×10^{-6} m^2/s) and acceleration due to gravity (9.81 m/s^2). Polyamide 12 particles with a Sauter mean diameter of 100 μm and a density of 1.016 g/cm^3 were used as flow tracers. A 2 mm laser plane generated by a double pulsed Nd:YAG 200 mJ laser across the channel's span at 40% of the flow depth (0.12 m) was used for illumination. Two synchronized Imager MX 4 MP cameras mounted below the flume captured 5000 images across an area of 0.44 m $\times$ 0.72 m at an acquisition frequency f = 50 Hz. PIV calculations were performed with LaVision's DaVis 8.0 software using multi-pass processing and image deformation techniques[53]. The multi-pass interrogation windows ranged from 64 px to 16 px having an overlap of 75%. Outliers in vectors were detected and removed using the PODDEM algorithm[34].

In addition, flow turbulence was measured in an empty flume, i.e., without patches. The streamwise and transverse turbulence intensities were determined to be 7.8% and 5.8% along the centerline. For all measurements reported, the origin of the coordinate system is located at the intersection of the laser plane and midpoint of the downstream edge of patches. The details regarding experimental set-up and visualization are summarized in Table I. As a remark on the geometries, the blockage ratio has been shown to have an effect on instabilities transitioning from being two-dimensional to three-dimensional due to wall-induced turbulence. However, this was shown not to be prominent up to a blockage ratio of 1/3 according to the Floquet stability analysis of Camarri and Giannetti [54], while the dimensions used in our study correspond to a value of 1/3. This will further be substantiated in our results, where we notice the absence of energetic scales of motion near the walls.

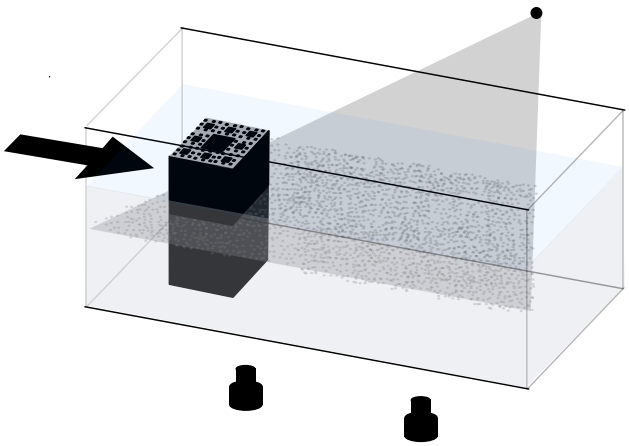

FIG. 2. Experimental setup showing the laser sheet and synchronized cameras at the bottom of the flume.

III. RESULTS AND DISCUSSION

A. Time-Averaging

The time-averaged statistics were calculated over a duration of 100 seconds. Figures 3(a-e) show contour plots of normalized mean velocity in the streamwise direction (x-direction), U/U_∞ with overlaid streamlines. Wakes due to porous patches are protracted and have a greater width compared to Case I, as reported previously by Nicolle and Eames[20], Taddei, Manes, and Ganapathisubramani[22], Nicolai *et al.*[23]. These findings are attributed to bleeding along the lateral and trailing edges. In the case of multi-scale porous patches, we observe contribution from individual elements in the near wake region, while these structures get encapsulated in the patch-scale wake further downstream. In Case III and Case V, element-scale wakes are associated with the second iteration, although the corresponding elements are not exactly located on the trailing edge. These flow perturbations do not dissipate within the patch and modify the near-wake characteristics. The near-wake region in Case IV contains element-scale perturbations introduced by the first iteration, which confirms the effect of configuration on the wake dynamics. The wake generated by single-scale porous patch (Case II) does not exhibit a strong flow reversal, which is explained as follows: extensive bleed flow through edges enhances momentum transfer between boundary layers around the patch and free-stream. This helps fluid in the vicinity of the patch to overcome adverse pressure gradient. In comparison, flow around the square cylinder separates at the

Seeding	Type	Polyamide powder
	Specific gravity	1.016 g/cm
	Diameter	100 μm
Light sheet	Laser type	Double pulsed Nd:YAG
	Maximum energy	200 mJ
	Wave length	532 nm
	Thickness	2 mm
Camera	Type	Imager MX 4M
	Resolution	2048 $\times$ 2048 px
	Pixel size	0.21 mm
	Lens focal length	24 mm
Imaging	Viewing area	440 mm $\times$ 440 mm
PIV Analysis	Interrogation area	final integration window size 16 px $\times$ 16 px
	Overlap	75%
	Approximate resolution	3.5 mm $\times$ 3.5 mm $\times$ 3.5 mm

TABLE I. Parameters corresponding to PIV setup.

leading edge and generates counter-rotating vortices which are shed periodically (not shown here). The near-wake region contains a recirculation zone caused by flow reversal associated with adverse pressure gradient.

We examine the lateral span of wake and its streamwise (x-direction) extent using wake momentum thickness defined as:

$$\Theta = \frac{1}{D}\int_{-\infty}^{+\infty} \frac{\overline{u}}{U_0}\Big(1 - \frac{\overline{u}}{U_0}\Big)\, dy \tag{1}$$

In the above equation, Θ is dimensionless from normalizing with the characteristic dimension of the square patch, D. As seen in Figure 4, the variation in Θ for multi-scale fractal patches is bounded by the two benchmark cases (Cases I & II). Θ drops to 0 rapidly at a short distance from the patch for square cylinder (Case I) compared to porous patches which show an extended wake region. The magnitude of wake momentum thickness corresponding to deterministic Sierpinski carpet (Case V) lies between Case III and Case IV. The single-scale patch shows almost a linear monotonic decrease due to extensive bleeding along the

edges compared to the other porous patches. Furthermore, points of inflection are present in the curves for porous patches (Figure 4) due to coexistence of element-scale and patch-scale signatures, which marginally accentuates the wake momentum thickness.

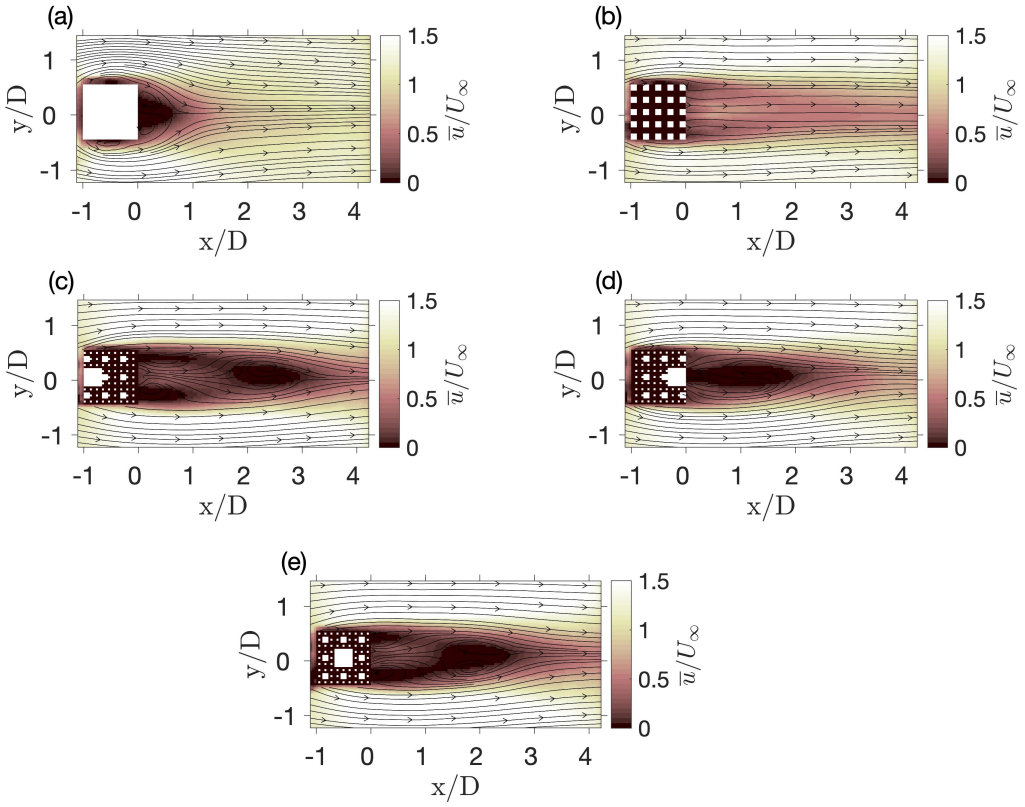

FIG. 3. Contour plots of mean resultant velocity normalized by inlet velocity with streamlines overlaid. Case I - (a), Case II - (b), Case III - (c), Case IV - (d), Case V - (e).

Next, we examine the distribution of normal (Figure 5) and shear Reynolds stresses (Figure 6). Turbulence kinetic energy (TKE) in Figure 5 is calculated as $1/2\ (\overline{u'^2} + \overline{v'^2})$, where u' and v' refer to velocity fluctuations in the streamwise (x) and spanwise (y) directions. In the wake of porous patches, the TKE distribution has noticeable element-scale features. Turbulence production occurs by perturbing a wider range of length scales based on the arrangement of iterations in these patches. In contrast, turbulence production in Case I relies predominantly on nonlinear cascade of primary vortex shedding in generating the scales of motion. The magnitude of TKE in the wake is the highest for Case I, while also having a significant distribution along the transverse edges around separation bubbles.

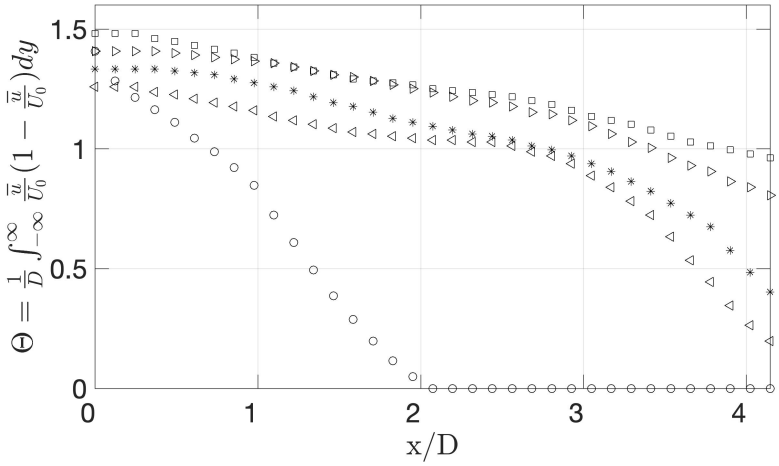

FIG. 4. Momentum thickness of wake downstream of obstacles: Case I - ∘, Case II - □, Case III - ▷, Case IV - ◁, Case V - ∗.

Case II has the least magnitude of TKE, which grows very slowly as we move downstream, reaching an asymptotic value before $x = 2D$. The values in Cases III-V are expected to lie in between the two benchmark cases in our field of view.

The normal Reynolds stresses do not appear to decay in the wake past porous patches (Figure 7). The streamwise (u, x-direction) turbulence intensity is higher than the transverse measure in the near-wake region (Figure 7a-c) due to bleed flow along the trailing edge. Here, the magnitude of $\overline{u'}/\overline{v'}$ is > 1 and drops as we move further downstream, where patch-scale dynamics become dominant. As a result, the ratio of intensities is < 1 and are identical for multi-scale fractal patches, while it is ~ 1 for the single-scale porous patch. In comparison, $\overline{u'}/\overline{v'}$ is always < 1 for the square cylinder. The fluctuations $\overline{u'}/\mathrm{U}_\infty$ and $\overline{v'}/\mathrm{U}_\infty$ however appear to homogenize for all the cases far downstream. Gomes-Fernandes, Ganapathisubramani, and Vassilicos[30], Hurst and Vassilicos[55] observed a similar homogenization behavior of larger scales after the point of maximum intensity in their fractal grids. However, the transport mechanisms in their studies are fundamentally different from turbulence generated using fractal patches. Flows past grids are symmetric about the streamwise axis, while fractal patches have standing cylinders whose one end is fixed and the free end is above the surface causing asymmetry in flow dynamics. Hence, we refrain from referring to the ratio of intensities as global isotropy factor, and we do not expect a linear combination of measured fluctuations to represent the third component.

Besides the roll-up of vortex sheets producing coherent fluid motion, instability in shear layers and the near-wake turbulence contribute to Reynolds stresses, and the resulting incoherent turbulence is more dominant at higher Reynolds numbers. Shear layers form unstable manifolds and produce a majority of incoherent structures affecting the TKE and Reynolds shear stress distribution in their vicinity[56,57]. The magnitude of $\overline{u'v'}$ is high along shear layers where turbulence transport is significant from entrainment of background flow. Turbulence due to amplification of shear layer instability propagates to the centerline at a short distance from the trailing edge in Case I affecting an anisotropic turbulence field with increase in $\overline{u'v'}$. This effect is significantly damped for the single-scale porous patch, where $\overline{u'}/\overline{v'} \sim 1$ persists along the centerline and away from shear layers. $\overline{u'v'}$ is relatively small in the near-wake region of porous patches. Though flow around individual elements within the patch adds to vorticity, their contribution rapidly attenuates due to vorticity annihilation, a phenomenon reported by Hunt and Eames[58], and observed previously for flow through array of elements[20,21]. However, beyond $x \sim 2D$, $\overline{u'v'}$ along the centerline is significantly different. Multi-scale excitation and interaction between the different modes of instability contribute to nonlinear growth of shear layers in the wake of multi-scale patches. The arrangement of elements clearly affects the Reynolds stress distribution, while the reason behind a prominent growth in Case V requires further investigation.

B. Proper Orthogonal Decomposition

We follow the work of Sirovich[59] for POD analysis. Using matrix notation, the decomposition is written as,

$$\mathbf{W} = \mathbf{\Phi}\,\mathbf{S}\,\mathbf{C}^{*} \tag{2}$$

$\mathbf{W}$ is an $I \times N$ matrix constructed using N temporally ordered snapshots of the flow-field. Since we are interested in the streamwise (x-direction) and spanwise (y-direction) evolution of the flow-field, $\mathbf{W}$ is formed by concatenating the respective velocity vectors as follows,

$$\mathbf{W}(I, 1, 2, \ldots N) = \begin{bmatrix} \mathbf{u}(X, 1, 2, \ldots N) \\ \mathbf{v}(X, 1, 2, \ldots N) \end{bmatrix} \tag{3}$$

The vectors $\mathbf{u}$ (x-direction) and $\mathbf{v}$ (y-direction) are fluctuating components obtained by

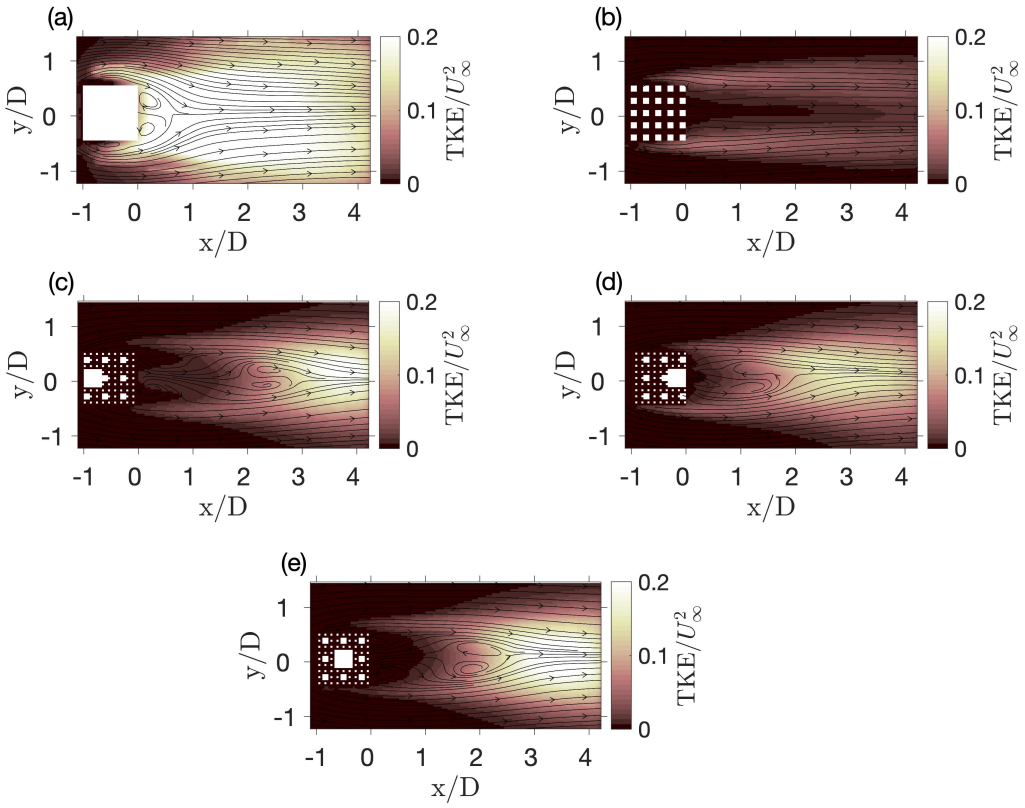

FIG. 5. Contour plots of turbulence kinetic energy normalized by the square of inlet velocity with streamlines overlaid. Case I - (a), Case II - (b), Case III - (c), Case IV - (d), Case V - (e).

subtracting the time-averaged mean value from PIV data. $Z = X \times Y$ is the total number of pixels in the x-y plane, and the number of rows in $\mathbf{W}$, $I = 2Z$. In this study, $X =$ 126 px, $Y = 205$ px, $I = 51660$ and $N = 5000$. $\mathbf{\Phi}$ appearing on the right hand side of Equation 2 is an orthonormal matrix with dimensions $I \times N$, and contains the spatial structure corresponding to Θ modes in the truncated transformation. As $I > N$ in our case, the number of modes determined from POD is $\Theta = N$. The respective temporal coefficients are present in the orthogonal matrix $\mathbf{C}$ (of size $\Theta \times \Theta$), and $\mathbf{C}^*$ is its conjugate transpose. $\mathbf{S}$ is a $\Theta \times \Theta$ matrix consisting of singular values of $\mathbf{W}$. The elements of $\mathbf{S}$ are then used to construct the vector, $\lambda = \text{diag}(\mathbf{S})^2/(N)$ whose components are proportional to modal turbulence kinetic energy, since we use fluctuating velocity components in $\mathbf{W}$. The elements in λ are arranged in decreasing order ($\lambda_1 \geq \lambda_2 \geq \ldots \lambda_\Theta \geq 0$), and their relative contribution shown in Figure 8 is evaluated as:

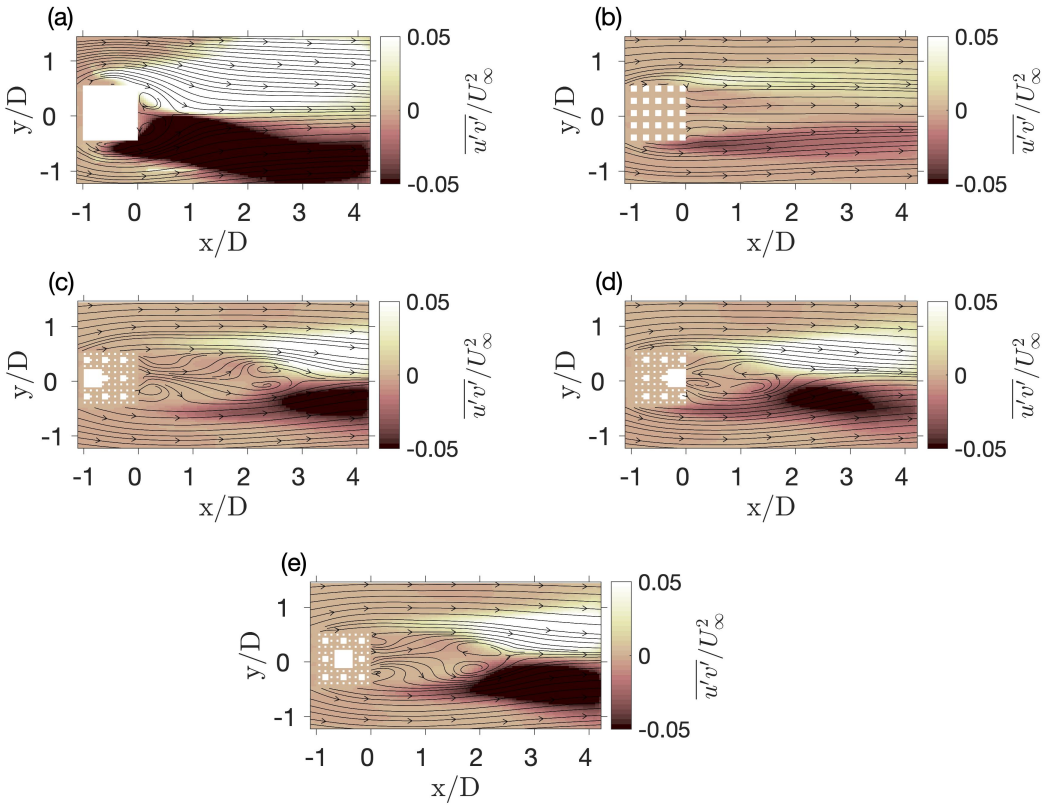

FIG. 6. Contour plots of off-diagonal Reynolds stress normalized by the square of inlet velocity with streamlines overlaid. Case I - (a), Case II - (b), Case III - (c), Case IV - (d), Case V - (e).

$$E_i(\%) = \frac{\lambda_i}{\sum_{i=1}^{\Theta} \lambda_i} \cdot 100 \tag{4}$$

E_i is proportional to the quasi two-dimensional turbulence kinetic energy in mode i, since we construct $\mathbf{W}$ using the streamwise (x-direction) and spanwise (y-direction) components.

The single-scale patch shows a distinct monotonous decrease in the modal energy content, resulting from persistent break-up of larger eddies into small-scale structures and lack of high-energy events in the wake. This corroborates the observations in Figure 7, where the fluctuations in the streamwise (x-direction) and spanwise (y-direction) directions have a similar magnitude for Case II. The solid square cylinder as well as the multi-scale patches have dominant contributions from the leading order modes due to high-energy events as discussed later. The energy content in individual modes are noticeably different (up to the fifth mode) between the multi-scale cases, highlighting the effect of the arrangement

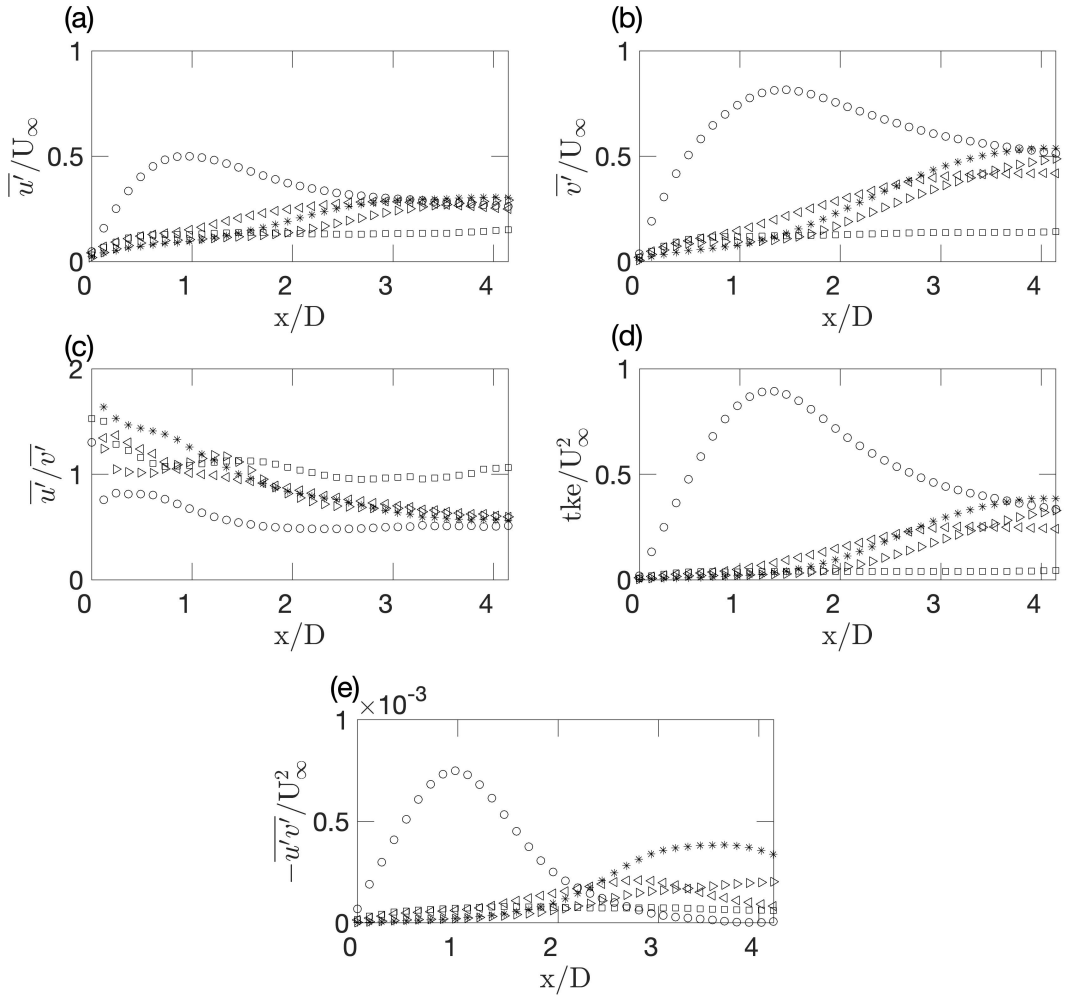

FIG. 7. Centerline variation of (a) streamwise (x-direction) turbulence intensity normalized by inlet velocity, (b) spanwise (y-direction) turbulence intensity normalized by inlet velocity, (c) ratio between streamwise (x-direction) and spanwise (y-direction) turbulence intensities, (d) turbulence kinetic energy normalized by the square of inlet velocity, (e) off-diagonal Reynolds stress normalized by the square of inlet velocity: Case I - $\circ$, Case II - $\square$, Case III - $\triangleright$, Case IV - $\triangleleft$, Case V - $*$.

of elements on the flow topology. We closely examine the first five spatial POD modes featuring structures emanating from correlated fluid motion or having identical dimensions and orientation in multiple snapshots.

The first two POD modes (Figure 9) reveal recirculation patterns associated with the largest spatial scales. Φ_1 alone is chosen for visualization, since Φ_2 closely resembles a conjugate pair of Φ_1, convecting larger scales in the streamwise direction[35]. This is evident from the

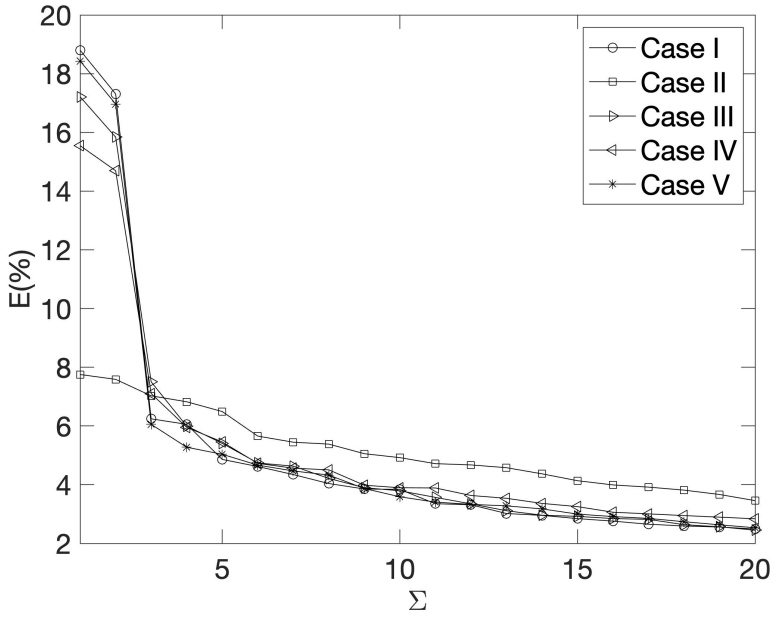

FIG. 8. Energy distribution in the first 20 POD modes.

shift in time series of temporal coefficients, while the Fourier spectra is identical between Φ_1 and Φ_2. There is a significant distribution of Φ_1 in the separation zones along the transverse edges in Case I. $C_{1,2}$ has a dominant Fourier component at the fundamental frequency close to St = 0.55. The modal energy contribution from Φ_1 in multi-scale patches is comparable to the case of square cylinder. The effects due to element-scale wakes are visible near the trailing edge, while patch-scale recirculation patterns appear further downstream in Cases III-V. In case III, where the largest scale is placed at the leading edge, the dominant frequency occurs at St = 0.80. As the largest iteration is moved to the center in the deterministic Sierpinski carpet (Case V), this frequency decreases to St = 0.75, while it drops to St = 0.65, where the largest iteration is at the trailing edge. On the other hand, Φ_1 distribution corresponding to the single-scale porous patch is remarkably different. Spatial development of shear layers from the edges and mixing of free-stream with transverse bleeding are prominent in this mode among other events. Flow perturbations introduced by elements are present although intermittent, which were not revealed by time-averaged statistics. Sub-harmonic contributions are present in addition to the fundamental frequency (St = 0.55) due to interactions between short-range element-scale wakes and bleeding along the trailing edge. The modal energy content in Φ_1 and Φ_2 are significantly less compared to

the square cylinder and multi-scale porous patches.

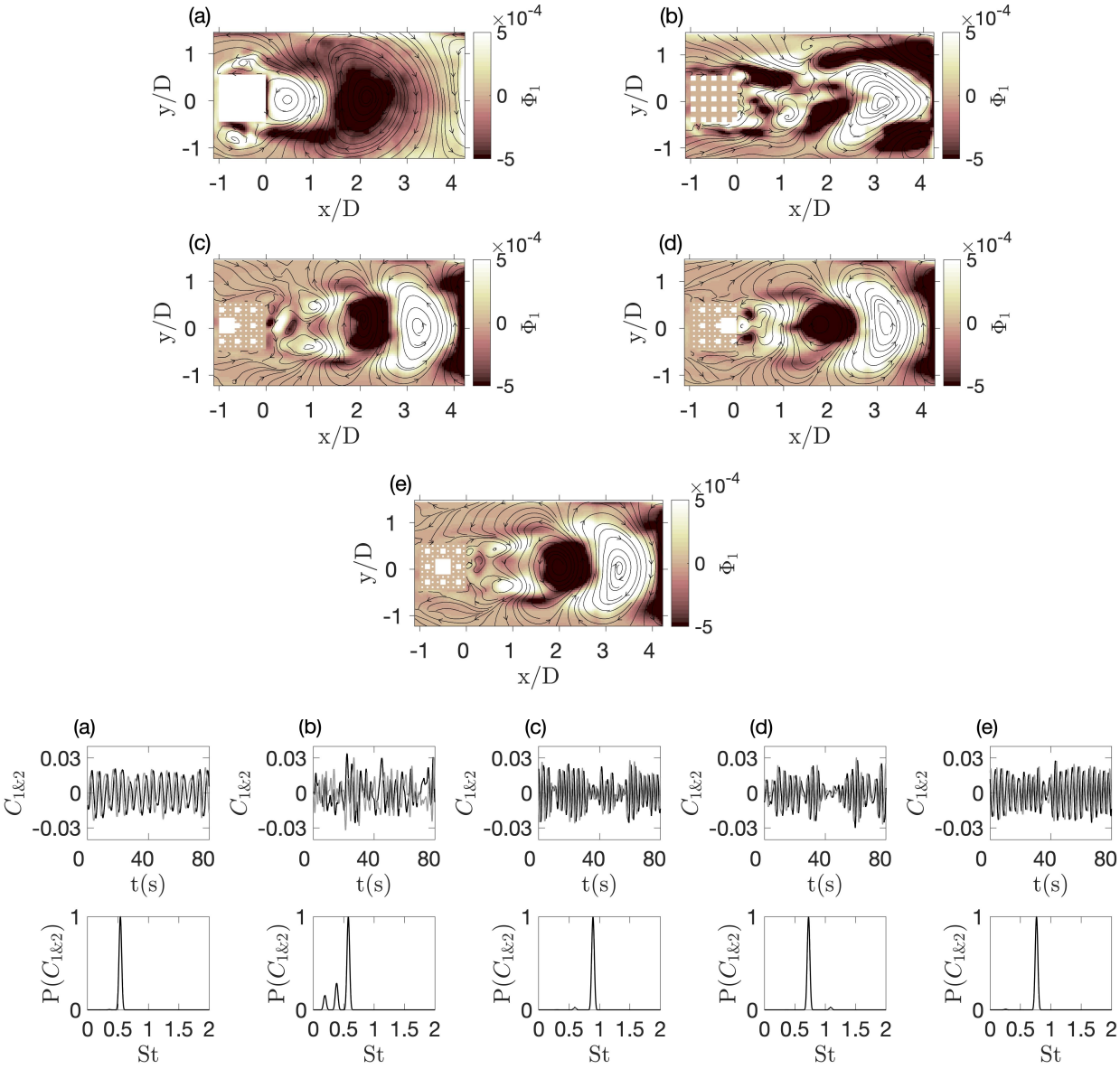

FIG. 9. The contours show POD spatial mode, Φ_1. The plots in the middle row contains temporal coefficients C_1, and the bottom row contains the corresponding Fourier spectra: (a) case I, (b) case II, (c) case III, (d) case IV and (e) case V.

Φ_3 (Figure 10) resembles the second harmonic in Case I and Case II as confirmed by the dominant frequency component, which occurs at St $\sim$ 1.1 and 1.2 respectively. We observe additional frequencies in both the cases though not as dominant. Features in Φ_3 distribution are streamwise-oriented in the neighborhood of local Φ_1 extrema appearing in Figure 9. These represent instabilities along the shear interface surrounding recirculation

patterns and the corresponding temporal coefficients have broader Fourier spectra. Such longitudinal features in higher-order POD modes were reported previously by Rehimi *et al.*[60] for single cylinders albeit much further downstream, and require several modes for accurate characterization.

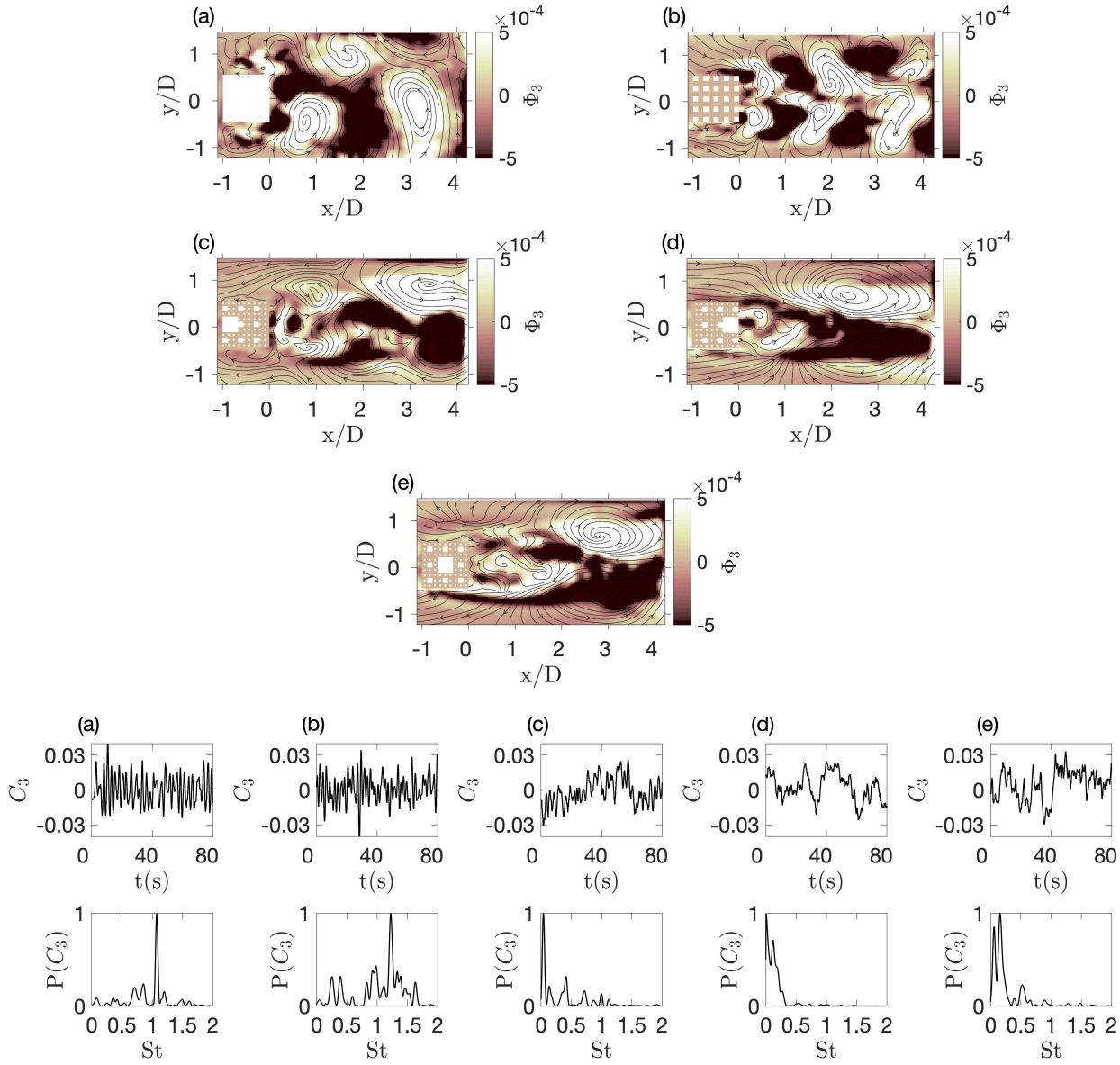

FIG. 10. The contours show the third POD spatial mode, Φ_3. The plots in the middle row contain temporal coefficients C_3, and the bottom row contains the corresponding Fourier spectra: (a) case I, (b) case II, (c) case III, (d) case IV and (e) case V.

Φ_4 (Figure 11) resembles a conjugate pair of Φ_3 for Cases I & II, while representing the second harmonic indicated by the respective dominant frequencies. Secondary peaks be-

come more prominent compared to C_3 due to the dynamics of smaller length-scales, for e.g., incoherent turbulence due to shear layer instability in Case I, and a combination of this with the evolution of element-scale wakes in Case II. For the multi-scale patches, Φ_4 distribution contains a combination of features from Φ_1 and Φ_3 and the corresponding temporal coefficient, C_4, has a broader frequency distribution whose Fourier spectra are colluded with multiple components similar to Cases I & II. Its distribution in Case IV does not contain prominent longitudinal structures compared to Cases III & V which is yet another evidence of dissimilarity in wake dynamics between the multi-scale patches.

Φ_5 (Figure 11) distribution reveals longitudinal structures in the single-scale porous patch, which were not present in the lower-order modes Φ_{1-4}. Flow perturbations due to individual elements are prominent along with instability occurring at the interface between their shear layers in the wake. The interaction between element-scale wake components are nonlinear as noticed previously and exhibit a complex interplay between vorticity annihilation and merging. The temporal coefficients C_5 contain a wide range of frequency components, evident in the $P(C_5)$ through multiple peaks. The distribution in the wake of a square cylinder is not markedly different compared to Φ_{1-4} having a dominant component at the second harmonic, along with a secondary peak at the sub-harmonic frequency. Φ_5 in multi-scale patches resembles a convected form of Φ_4. In fact, the frequency distribution in $P(C_4)$ and $P(C_5)$ appear almost identical in Cases IV & V besides subtle differences in their magnitudes. In Case III, a dominant component corresponding to sub-harmonic frequency is lost, and the distribution is colluded with high frequency components, albeit the location of primary peak remains intact. It is safe to conclude that $\Phi_{4\&5}$ resemble a conjugate pair with respect to the energetic scales of motion.

Thus, POD provides more granularity to element-scale and patch-scale dynamics through interpretation of different instability modes, which were not apparent from time-averaged statistics. The five POD modes examined in this study accounts for $\sim 50\%$ of the total energy, and several additional modes are required for a higher resolution of the flow-field. We restrict our analysis to the first few modes to highlight the different nonlinear mechanisms, of which the most dominant ones may be attributed to the time-averaged description provided earlier. We notice significant difference in the distribution of spatial modes between the multi-scale patches resulting from the configuration of elements. The modal energy content in the near-wake region is strongly characterized by the iterations placed closest to the

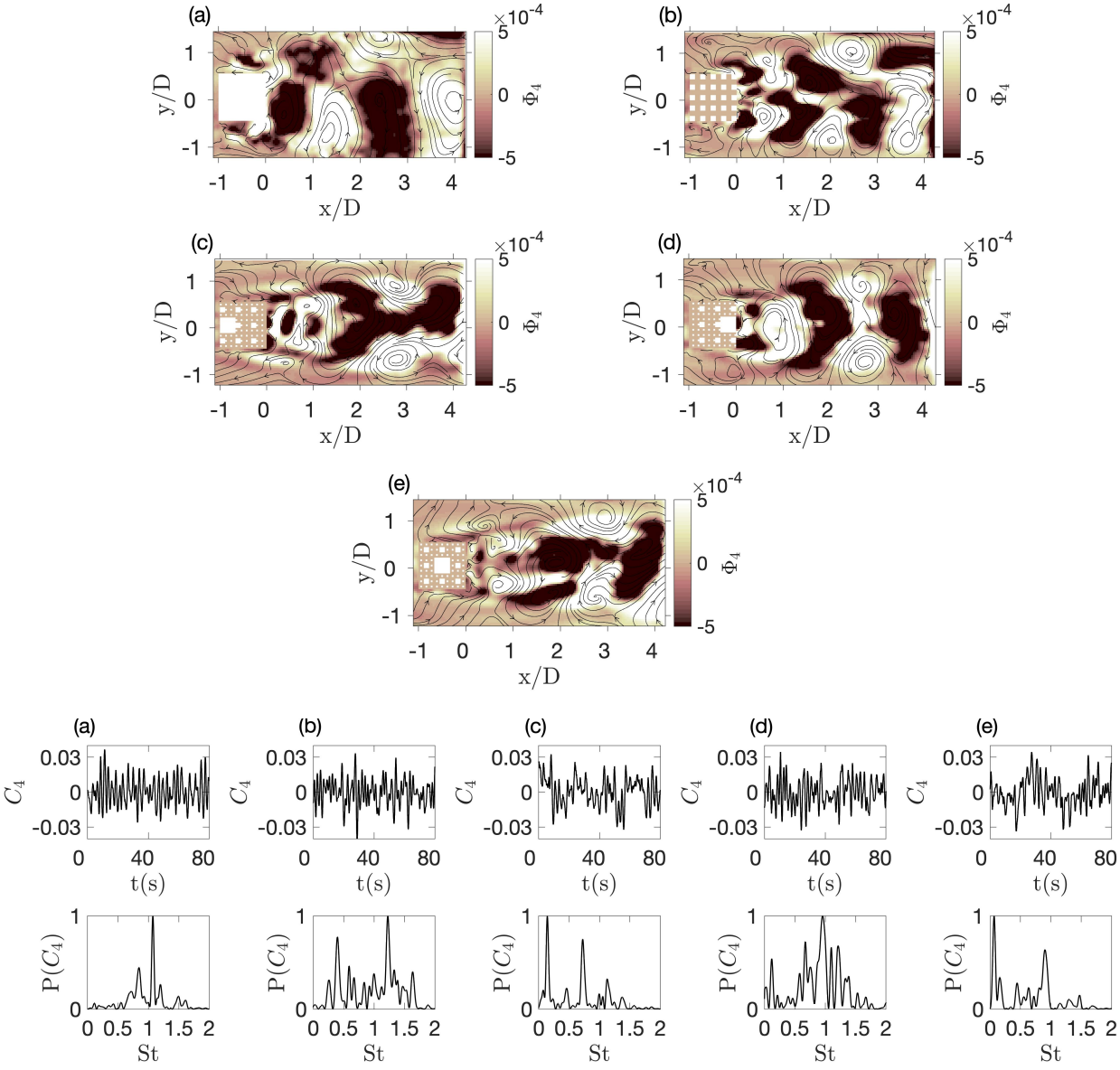

FIG. 11. The contours show the fourth POD spatial mode, Φ_4. The plots in the middle row contain temporal coefficients C_4, and the bottom row contains the corresponding Fourier spectra: (a) case I, (b) case II, (c) case III, (d) case IV and (e) case V.

trailing edge, which also determines the rate of bleeding and affects the wake dimensions. It is worth stressing that structures featuring in spatial POD modes may not necessarily translate to physical flow structures in experiments. The flow-field results from the modulation of spatial functions by temporal coefficients. Also, the statistics are affected by higher-order modes associated with mechanisms such as generation of asymmetric vortices or shear-induced secondary instabilities, which are substantial in our case.

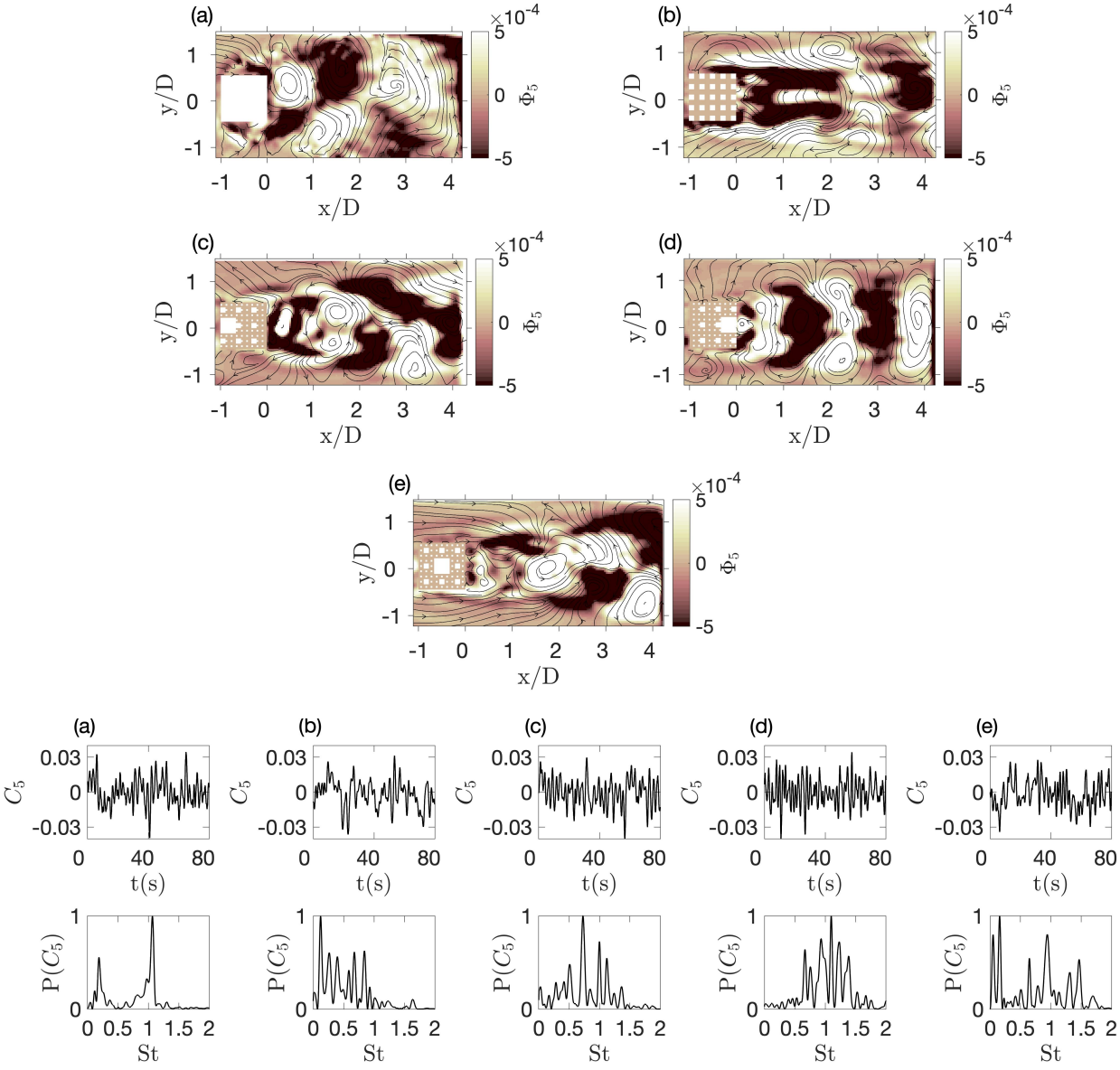

FIG. 12. The contours show the fifth POD spatial mode, Φ_5. The plots in the middle row contain temporal coefficients C_5, and the bottom row contains the corresponding Fourier spectra: (a) case I, (b) case II, (c) case III, (d) case IV and (e) case V.

C. Dynamic Mode Decomposition

Finally, we apply DMD to further characterize the underlying dynamics. We follow the method of Schmid[38], Tu *et al.*[39] where two sub-datasets of $\mathbf{W}$ are formed as follows,

$$\mathbf{W}_1 = \mathbf{W}(I; 1, 2, \ldots T-1) \quad \& \quad \mathbf{W}_2 = \mathbf{W}(I; 2, 3, \ldots T) \tag{5}$$

$\mathbf{W}_1$ and $\mathbf{W}_2$ are $I \times (N-1)$ matrices. The singular value decomposition of $\mathbf{W}_1$ is formulated as,

$$\mathbf{W}_1 = \hat{\mathbf{\Phi}}\,\hat{\mathbf{S}}\,\hat{\mathbf{C}}^* \tag{6}$$

where $\hat{}$ denotes the use of sub-dataset instead of entire columns of our data matrix. $\hat{\mathbf{\Phi}}$, $\hat{\mathbf{S}}$ and $\hat{\mathbf{C}}$ have dimensions $I \times (N-1)$, $(N-1) \times (N-1)$ and $(N-1) \times (N-1)$ respectively. We generate the pseudo-Arnoldi operator $\mathbf{A}$ which is an $(N-1) \times (N-1)$ matrix as follows,

$$\mathbf{A} = \hat{\mathbf{\Phi}}^T \mathbf{W}_2 \hat{\mathbf{C}} \hat{\mathbf{S}}^{-1} \tag{7}$$

having eigenvalues β and eigenvectors $\mathbf{Y}$. The following transformation is applied to obtain frequencies from eigenvalues[35,40]:

$$\mathbf{G} = \mathrm{f}\arg(\beta)/2\pi \tag{8}$$

$\mathbf{G}$ is a real-valued vector whose elements are now comparable to frequencies from our POD analysis. In fact, we use dominant frequencies corresponding to leading POD modes to search for the corresponding eigenvector $\mathbf{Y_i}$, eventually used to generate the vectorized DMD mode $\mathbf{\Psi}$ as follows[35],

$$\mathbf{\Psi} = \hat{\mathbf{\Phi}}\mathbf{Y}_i, \tag{9}$$

We construct the first DMD mode, $\mathbf{\Psi_1}$ shown in Figure 13 using the dominant frequencies from $\mathbf{\Phi_1}$. The support of this mode appears similar to $\mathbf{\Phi_1}$ distribution (Figure 9) except for Case II. The disparity can be explained by the presence of sub-harmonics in the Fourier spectra of single-scale porous patch, while the other cases have a distinct dominant frequency. This confirms the largest scales of motion are not just spatially relevant but spatio-temporally perspective for the square cylinder and multi-scale patches. Also, we note that the support of $\mathbf{\Psi_1}$ exists in shear layers and wake in these cases. Since a DMD mode corresponds to a single frequency, this could indicate possible phase-locking between the associated mechanisms[39]. The large-scale vortex shedding is quenched in the near-wake region of porous patches due to bleed flow while exciting the far-wake modes, contributing to patch-scale dynamics.

We then examine the second DMD mode, $\mathbf{\Psi_2}$ (Figure 14) by isolating the harmonic frequency in each case. $\mathbf{\Psi_2}$ distribution is remarkably similar in the wakes of all patches although the large-scale spatio-temporal coherent structures identified by $\mathbf{\Phi_1}$ and $\mathbf{\Psi_1}$ are disparate. The secondary structures emanating from primary instabilities have identical temporal response which highlights the nature of incoherent turbulence from vortex stretching by manifolds. Furthermore, distributions of $\mathbf{\Phi_3}$ and $\mathbf{\Psi_2}$ are identical for Cases I & II, suggestive of spatially and temporally relevant structures corresponding to their second harmonic. The dominant features seen in $\mathbf{\Psi_2}$ are not present in $\mathbf{\Phi_3}$, which implies the temporally relevant scales of motion do not necessarily represent high-energy events. Also, the near-wake and far-wake regions have a similar $\mathbf{\Psi_2}$ distribution unlike $\mathbf{\Psi_1}$.

Overall, we find results from DMD to supplement our findings from POD. The arrangement of iterations affects the spatio-temporal evolution of flow past porous patches. We find further evidence of co-existing near-wake and far-wake regions characterized by nonlinear interactions between element-scale and patch-scale dynamics. While DMD alone is not sufficient to elucidate the complex dynamics, along with POD, it provides useful insights into development of energetic scales of motion. Furthermore, we find the combination of POD and DMD to distinguish between coherent and incoherent fluctuating fields qualitatively.

IV. CONCLUSION

We identify dynamical features associated with flow through and around porous patches comprised of single-scale and multi-scale elements. The arrangement of iterations within the patch clearly has an effect on the wake characteristics, especially the ones placed closer to the trailing edge. Element-scale perturbations attenuate depending on their location and dimensions, which may persist in the near-wake region. However, an encapsulating patch-scale wake is present in all the cases, which is protracted and enlarged in the spanwise direction compared to the wake behind a square cylinder. This is a result of bleeding through transverse and trailing edges. In porous patches, turbulence is generated by multi-scale excitation as flow passes through different elements, and the element-scale wakes interact to alter the dynamics in the near-wake region. Further downstream, the separated shear layers from the edges grow, become unstable and develop secondary instabilities. The complex nature of interactions between these nonlinear mechanisms is further described using POD

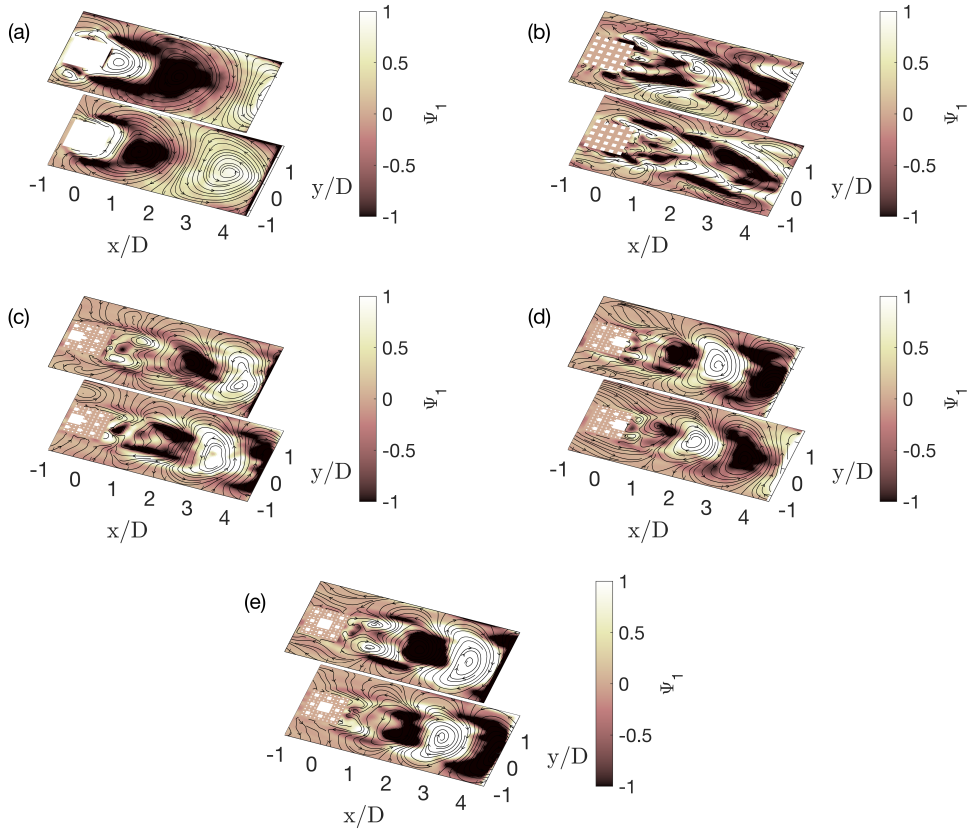

FIG. 13. The contours show the real (top) and imaginary (bottom) parts of DMD mode corresponding to the first harmonic, Ψ_1. (a) case I, (b) case II, (c) case III, (d) case IV and (e) case V.

analysis. The modal energy content is significantly different for the single-scale porous patch which exhibits a monotonic decrease. Also, the lower-order spatial modes are not as energetic compared to the other cases, while the higher-order modes have similar magnitudes. $\Phi_{1\&2}$ resemble a conjugate pair for all the cases and the dominant frequencies are modified by the placement of iterations within the patch. $\Phi_{3\&4}$ resemble a conjugate pair for Cases I & II, while the dominant frequency occurs at the second harmonic, although the spectra are colluded with multiple components. Similarly, $\Phi_{4\&5}$ resemble a conjugate pair for the multi-scale patches while describing the energetic scales of motion. In these cases, higher-order modes feature longitudinal structures surrounding local extrema in Φ_1. Their spatial support and dominant frequencies corresponding to their temporal coefficients are remark-

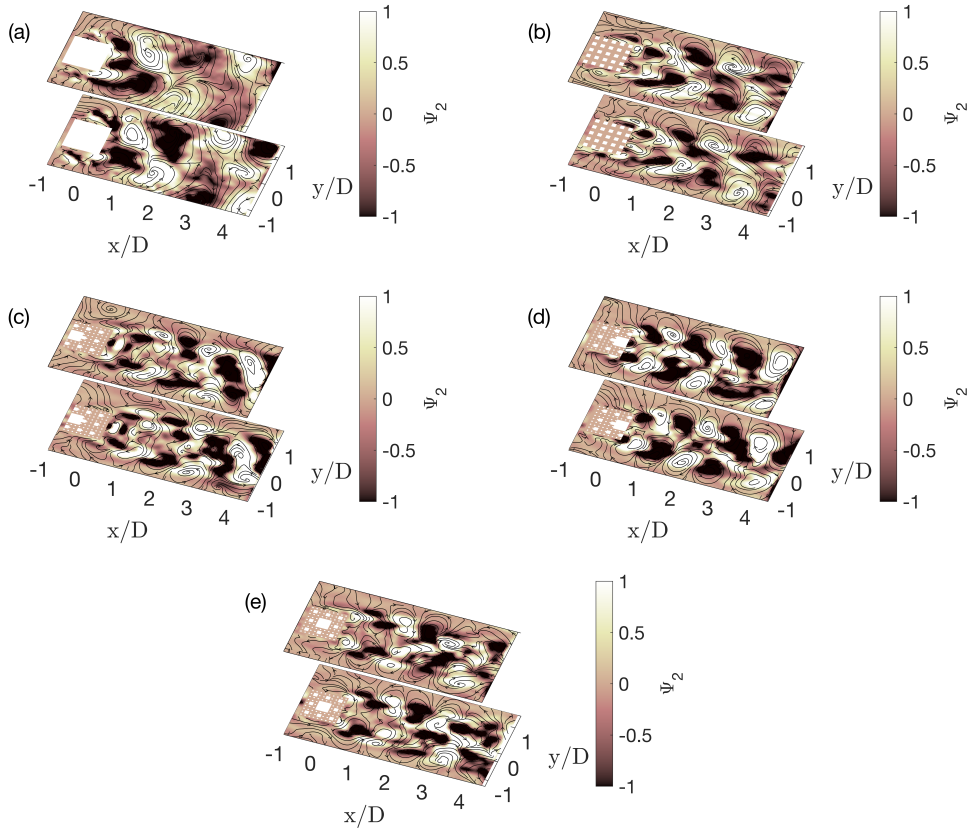

FIG. 14. The contours show the real (top) and imaginary (bottom) parts of DMD mode corresponding to the second harmonic, Ψ_2. (a) case I, (b) case II, (c) case III, (d) case IV and (e) case V.

ably different. We then apply DMD to study the temporally relevant structures. The first DMD mode Ψ_1 resembles Φ_1 for all patches except the single-scale porous patch, and Ψ_2 is identical for all the cases. The study presents a successful application of POD and DMD to characterize element-scale and patch-scale dynamics in the wakes of porous patches and provide a qualitative distinction between coherent and incoherent turbulence.

V. DATA AVAILABILITY STATEMENT

The data that support the findings of this study are available from the corresponding author upon reasonable request.

REFERENCES

[1]B. B. Mandelbrot, *The fractal geometry of nature*, Vol. 2 (W.H. Freeman, 1982).

[2]M. Batty and P. A. Longley, *Fractal cities: A geometry of form and function* (Academic Press, 1994).

[3]C. Vanderwel and B. Ganapathisubramani, "Turbulent boundary layers over multiscale rough patches," Boundary-Layer Meteorology **172**, 1–16 (2019).

[4]E. R. Micheli and J. W. Kirchner, "Effects of wet meadow riparian vegetation on streambank erosion. 1. remote sensing measurements of streambank migration and erodibility," Earth Surface Processes and Landforms **27**, 627–639 (2002), https://onlinelibrary.wiley.com/doi/pdf/10.1002/esp.338.

[5]K. Gedan, M. Kirwan, E. Wolanski, E. Barbier, and B. Silliman, "The present and future role of coastal wetland vegetation in protecting shorelines: Answering recent challenges to the paradigm," Climatic Change **106**, 7–29 (2010).

[6]R. J. Wilcock, P. D. Champion, J. W. Nagels, and G. F. Croker, "The influence of aquatic macrophytes on the hydraulic and physico-chemical properties of a new zealand lowland stream," Hydrobiologia **416**, 203–214 (1999).

[7]H. Nepf, "Drag, turbulence, and diffusion in flow through emergent vegetation," Water Resources Research **35**, 479–489 (1999).

[8]M. Schulz, H.-P. Kozerski, T. Pluntke, and K. Rinke, "The influence of macrophytes on sedimentation and nutrient retention in the lower river spree (germany)," Water Research **37**, 569–578 (2003).

[9]M. Zdravkovich, "Review—review of flow interference between two circular cylinders in various arrangements," Journal of Fluids Engineering **99**, 618–633 (1977).

[10]M. Zdravkovich, "The effects of interference between circular cylinders in cross flow," Journal of Fluids and Structures **1**, 239–261 (1987).

[11]D. Sumner, S. Price, and M. Paigdoussis, "Investigation of side-by-side circular cylinders in steady cross-flow by particle image velocimetry," in *Proceedings 1998 ASME Fluids Eng. Division Summer Meeting* (1998).

[12]D. Sumner, S. Wong, S. Price, and M. Paidoussis, "Fluid behaviour of side-by-side circular cylinders in steady cross-flow," Journal of Fluids and Structures **13**, 309–338 (1999).

[13]D. Sumner, "Two circular cylinders in cross-flow: a review," Journal of Fluids and Structures **26**, 849–899 (2010).

[14]V. Kolar, D. Lyn, and W. Rodi, "Ensemble-averaged measurements in the turbulent near wake of two side-by-side square cylinders," Journal of Fluid Mechanics **346**, 201–237 (1997).

[15]H. Wang and Y. Zhou, "The finite-length square cylinder near wake," Journal of Fluid Mechanics **638**, 453–490 (2009).

[16]G. J. Sheard, M. J. Fitzgerald, and K. Ryan, "Cylinders with square cross-section: wake instabilities with incidence angle variation," Journal of Fluid Mechanics **630**, 43 (2009).

[17]M. M. Alam, Y. Zhou, and X. Wang, "The wake of two side-by-side square cylinders," Journal of Fluid Mechanics **669**, 432–471 (2011).

[18]M. M. Alam, H. Bai, and Y. Zhou, "The wake of two staggered square cylinders," Journal of Fluid Mechanics **801**, 475–507 (2016).

[19]H. Bai and M. M. Alam, "Dependence of square cylinder wake on reynolds number," Physics of Fluids **30**, 015102 (2018).

[20]A. Nicolle and I. Eames, "Numerical study of flow through and around a circular array of cylinders," Journal of Fluid Mechanics **679**, 1–31 (2011).

[21]L. Zong and H. Nepf, "Vortex development behind a finite porous obstruction in a channel," Journal of Fluid Mechanics **691**, 368–391 (2012).

[22]S. Taddei, C. Manes, and B. Ganapathisubramani, "Characterisation of drag and wake properties of canopy patches immersed in turbulent boundary layers," Journal of Fluid Mechanics **798**, 27–49 (2016).

[23]C. Nicolai, S. Taddei, C. Manes, and B. Ganapathisubramani, "Wakes of wall-bounded turbulent flows past patches of circular cylinders," Journal of Fluid Mechanics **892** (2020).

[24]D. Queiros-Conde and J. Vassilicos, "Turbulent wakes of 3d fractal grids," in *Intermittency in turbulent flows*, edited by J. C. Vassilicos (Cambridge University Press, Cambridge, UK, 2001) pp. 136–167.

[25]B. Mazzi, F. Okkels, and J. Vassilicos, "A shell-model approach to fractal-induced turbulence," The European Physical Journal B-Condensed Matter and Complex Systems **28**, 243–251 (2002).

[26]A. Staicu, B. Mazzi, J. Vassilicos, and W. van de Water, "Turbulent wakes of fractal objects," Physical Review E **67**, 066306 (2003).

[27]B. Mazzi and J. Vassilicos, "Fractal-generated turbulence," Journal of Fluid Mechanics **502**, 65–87 (2004).

[28]L. Biferale, A. S. Lanotte, and F. Toschi, "Effects of forcing in three-dimensional turbulent flows," Physical Review Letters **92**, 094503 (2004).

[29]A. K. Kuczaj, B. J. Geurts, and W. D. McComb, "Nonlocal modulation of the energy cascade in broadband-forced turbulence," Physical Review E **74**, 016306 (2006).

[30]R. Gomes-Fernandes, B. Ganapathisubramani, and J. Vassilicos, "Particle image velocimetry study of fractal-generated turbulence," Journal of Fluid Mechanics **711**, 306–336 (2012).

[31]W. Sierpinski, "Sur une courbe cantorienne qui contient une image biunivoque et continue de toute courbe donnée," Comptes Rendus **629** (1916).

[32]H. Jiang and L. Cheng, "Flow separation around a square cylinder at low to moderate reynolds numbers," Physics of Fluids **32**, 044103 (2020), https://doi.org/10.1063/5.0005757.

[33]C. Williamson, "Three-dimensional wake transition," in *Advances in Turbulence VI* (Springer, 1996) pp. 399–402.

[34]J. Higham, W. Brevis, and C. Keylock, "A rapid non-iterative proper orthogonal decomposition based outlier detection and correction for PIV data," Measurement Science and Technology **27**, 125303 (2016).

[35]J. E. Higham, W. Brevis, C. Keylock, and A. Safarzadeh, "Using modal decompositions to explain the sudden expansion of the mixing layer in the wake of a groyne in a shallow flow," Advances in Water Resources (2017).

[36]J. Higham, A. Vaidheeswaran, K. Benavides, and P. Shepley, "Eigenparticles: characterizing particles using eigenfaces," Granular Matter **21**, 45 (2019).

[37]J. E. Higham, M. Shahnam, and A. Vaidheeswaran, "Using a proper orthogonal decomposition to elucidate features in granular flows," Granular Matter **22**, 2979–2995 (2020).

[38]P. J. Schmid, "Dynamic mode decomposition of numerical and experimental data," Journal of Fluid Mechanics **656**, 5–28 (2010).

[39]J. H. Tu, C. W. Rowley, D. M. Luchtenburg, S. L. Brunton, and J. N. Kutz, "On dynamic mode decomposition: Theory and applications," arXiv preprint arXiv:1312.0041 (2013).

[40]J. Higham and W. Brevis, "Modification of the modal characteristics of a square cylinder wake obstructed by a multi-scale array of obstacles," Experimental Thermal and Fluid

Science **90**, 212–219 (2018).

[41]K. Taira, S. L. Brunton, S. T. Dawson, C. W. Rowley, T. Colonius, B. J. McKeon, O. T. Schmidt, S. Gordeyev, V. Theofilis, and L. S. Ukeiley, "Modal analysis of fluid flows: An overview," Aiaa Journal **55**, 4013–4041 (2017).

[42]J. Wang, G. Huang, W. Lu, and P. E. Sullivan, "Dynamic mode decomposition analysis of flow separation in a diffuser to inform flow control strategies," Journal of Fluids Engineering **142** (2020).

[43]K. Taira, M. S. Hemati, S. L. Brunton, Y. Sun, K. Duraisamy, S. Bagheri, S. T. Dawson, and C.-A. Yeh, "Modal analysis of fluid flows: Applications and outlook," AIAA journal **58**, 998–1022 (2020).

[44]K. Bhavithavya Kidambi, W. MacKunis, S. V. Drakunov, and V. Golubev, "Sliding mode estimation and closed-loop active flow control under actuator uncertainty," International Journal of Robust and Nonlinear Control **30**, 6645–6660 (2020).

[45]B. Herrmann, P. J. Baddoo, R. Semaan, S. L. Brunton, and B. J. McKeon, "Data-driven resolvent analysis," arXiv preprint arXiv:2010.02181 (2020).

[46]D. Bhattacharjee, B. Klose, G. B. Jacobs, and M. S. Hemati, "Data-driven selection of actuators for optimal control of airfoil separation," Theoretical and Computational Fluid Dynamics **34**, 557–575 (2020).

[47]A. Vaidheeswaran and M. L. de Bertodano, "Stability and convergence of computational eulerian two-fluid model for a bubble plume," Chemical Engineering Science **160**, 210–226 (2017).

[48]W. D. Fullmer and C. M. Hrenya, "The clustering instability in rapid granular and gas-solid flows," Annual Review of Fluid Mechanics **49**, 485–510 (2017).

[49]L. De Martín, C. Ottevanger, J. R. Van Ommen, and M.-O. Coppens, "Universal stability curve for pattern formation in pulsed gas-solid fluidized beds of sandlike particles," Physical Review Fluids **3**, 034303 (2018).

[50]A. Vaidheeswaran, A. Clausse, W. D. Fullmer, R. Marino, and M. L. de Bertodano, "Chaos in wavy-stratified fluid-fluid flow," Chaos: An Interdisciplinary Journal of Nonlinear Science **29**, 033121 (2019).

[51]A. Vaidheeswaran and S. Rowan, "Chaos and recurrence analyses of pressure signals from bubbling fluidized beds," Chaos, Solitons & Fractals **142**, 110354 (2021).

[52]A. Clausse and M. L. de Bertodano, "Natural modes of the two-fluid model of two-phase flow," arXiv preprint arXiv:2101.06339 (2021).

[53]F. Scarano, "Iterative image deformation methods in PIV," Measurement Science and Technology **13**, R1 (2002).

[54]S. Camarri and F. Giannetti, "Effect of confinement on three-dimensional stability in the wake of a circular cylinder," Journal of Fluid Mechanics **642**, 477 (2010).

[55]D. Hurst and J. Vassilicos, "Scalings and decay of fractal-generated turbulence," Physics of Fluids (1994-present) **19**, 035103 (2007).

[56]W. Reynolds and A. Hussain, "The mechanics of an organized wave in turbulent shear flow. part 3. theoretical models and comparisons with experiments," Journal of Fluid Mechanics **54**, 263–288 (1972).

[57]B. Cantwell and D. Coles, "An experimental study of entrainment and transport in the turbulent near wake of a circular cylinder," Journal of Fluid Mechanics **136**, 321–374 (1983).

[58]J. Hunt and I. Eames, "The disappearance of laminar and turbulent wakes in complex flows," Journal of Fluid Mechanics **457**, 111–132 (2002).

[59]L. Sirovich, "Turbulence and the dynamics of coherent structures. i-coherent structures. ii-symmetries and transformations. iii-dynamics and scaling," Quarterly of Applied Mathematics **45**, 561–571 (1987).

[60]F. Rehimi, F. Aloui, S. B. Nasrallah, L. Doubliez, and J. Legrand, "Experimental investigation of a confined flow downstream of a circular cylinder centred between two parallel walls," Journal of Fluids and Structures **24**, 855–882 (2008).